RSC Advances

PAPER

View Article Online
View Journal | View Issue

Cite this: *RSC Adv.*, 2024, **14**, 9869

Effect of CeO_2 support structure on the catalytic performance of ammonia synthesis in an electric field at low temperatures†

Ryuku Maeda,[a] Hiroshi Sampei,[a] Reika Nakayama,[a] Takuma Higo,[a] Yoshiki Koshizuka,[a] Yoshiro Bando,[b] Tasuku Komanoya,[b] Yunosuke Nakahara[b] and Yasushi Sekine *[a]

Received 25th February 2024
Accepted 15th March 2024

DOI: 10.1039/d4ra01457j

rsc.li/rsc-advances

Ammonia is an extremely important storage and transport medium for renewable energy, and technology is expected to produce it on demand and onsite using renewable energy. Applying a DC (direct current) to a solid catalyst layer with semiconducting properties makes ammonia synthesis highly efficient, even at low temperatures (approximately 400 K). In this process, oxide supports with semiconducting properties play important roles as metal supports and conduction fields for electrons and protons. The influence of the degree of particle aggregation on the support properties and ammonia synthesis using an electric field was evaluated for CeO_2, which is the best material for this purpose because of its semiconducting properties. The results showed that controlling the aggregation structure of the crystalline particles could significantly influence the surface conductivity of protons and electrons; thus, the activity could be largely controlled. The Ru–CeO_2 interaction could also be controlled by changing the crystallinity, which suppressed the aggregation of the supported Ru and significantly improved the ammonia synthesis activity using an electric field at low temperatures.

1 Introduction

Recently, hydrogen energy has attracted attention as an alternative energy source to fossil fuels, with the continued research on processes to convert renewable energy into hydrogen energy for storage and transportation.[1,2] In particular, ammonia (NH_3) is a promising hydrogen carrier because it has a high hydrogen density (17.8 wt%), is carbon-free and is easy to liquefy and handle.[3] Because NH_3 production using renewable energy must adapt to its temporal and spatial fluctuations, an on-site NH_3 production method that can be driven under milder conditions (lower temperature and lower pressure) than that of conventional methods is needed.[4] Recently, we have discovered that low-temperature, low-pressure NH_3 synthesis can be achieved *via* a catalytic reaction in an electric field (EF) in which a DC (direct current) is applied to a semiconducting catalyst support.[5–8] In this reaction, the applied current induces proton conduction on the surface of the support (surface protonics), which promotes the dissociation of the N≡N bond *via* proton collisions and intermediate formation, even at low temperatures.[5,6] In the NH_3 synthesis reaction with an EF *via* the N_2H intermediate, which is formed from the reaction of protons conducted on the support with N_2 molecules on the active metal, surface protonics enables a lower reaction temperature. Hydrogen spillover is a similar phenomenon known as proton migration at the catalyst surface, in which protons on the catalyst surface and electrons inside the catalyst are coupled and transferred *via* a hydrogen concentration gradient on the surface.[9–11] In the reaction with an EF, the electrons are forced to move *via* the applied DC, which can be considered as driving hydrogen spillover.[12–15] Thus, the conductivity of protons at the surface of the catalyst support is an important property that affects the reaction with EFs.

Generally, catalyst supports can regulate the charge of the active metals in the catalytic reaction field and inhibit thermal aggregation owing to the active metal–metal binding.[16,17] In the NH_3 synthesis reaction, these support properties can be simultaneously expressed with the EF to develop high-performance catalysts. Owing to its oxygen storage, redox, and oxygen ion conductivity, CeO_2 is a metal oxide used as a catalyst not only for NH_3 synthesis but also for a wide range of reactions, such as automotive exhaust gas purification, water gas shift, steam reforming, and CO oxidation. CeO_2 can promote various reactions by changing the molecular adsorption strength and oxygen deficiency concentration by varying the exposure surface.[18–30] Although there have been studies on doping heterogeneous cations in CeO_2 to change their support

[a]*Department of Applied Chemistry, Waseda University, 3-4-1, Okubo, Shinjuku, 169-8555, Tokyo, Japan. E-mail: ysekine@waseda.jp*

[b]*Mitsui Mining and Smelting Co. Ltd, 1333-2, Haraichi, Ageo, 362-0021, Saitama, Japan*

† Electronic supplementary information (ESI) available. See DOI: https://doi.org/10.1039/d4ra01457j

properties and improve the performance of NH_3 synthesis reactions, no examples of changing the crystalline state of the same oxide to provide new support properties have been reported. In this study, two types of CeO_2 (CeO_2-p and CeO_2-s) with different degrees of crystal aggregation were used. These have almost the same purity but different micro-crystalline structures. These were used to investigate the effect of the support crystal agglomeration on the surface ionic conductivity and ammonia synthesis activity. For the two samples used in this study, CeO_2-p had a higher crystal orientation than CeO_2-s. The ratio of hydroxyl groups-to-Ce^{3+} on their surfaces was equal, and the number of spillover carriers was the same. However, AC impedance measurements revealed that CeO_2-p had higher proton conductivity than CeO_2-s. In addition, CO pulse measurements revealed that CeO_2-p had a strong Ru particle–CeO_2 interaction, which kept the Ru particles highly dispersed with a longer interface length. Theoretical calculations indicated that this interaction was due to CeO_2-p exposing (100) planes with high surface energy. Owing to the concerted effect of high proton conductivity and a longer interface length, CeO_2-p was more active than CeO_2-s in NH_3 synthesis with EFs.

2 Experimental

2.1 Catalyst preparation

All catalysts were supported on two types of CeO_2 oxides. CeO_2-p, supplied by Mitsui Mining and Smelting Co., Ltd, and CeO_2-s, provided by JRC (Japan Reference Catalyst) were used for comparison; both of them have high purity in the CeO_2 contents. These two oxides have different migrated crystal structures. Ru particle was loaded onto the two CeO_2 particles using an evaporation–drying method with an aqueous solution of $Ru(NO_3)_3$, Tanaka Precious Metals. The sample was then stirred 100 rpm for 2 h while deaerating. The sample was then transferred to an evaporating dish, evaporated to dryness on a hot stirrer at about 100 °C and dried in an oven at 120 °C for 24 hours. The resulting powder was treated at 450 °C, 10 °C min^{-1}, 2 h, in $H_2:Ar = 1:1$ (total 100 SCCM). Finally, the catalyst powder was moulded in a pressure moulding machine at 60 kN for 15 min to obtain a particle size of 355–500 μm. As Ru is easily oxidised in air, hydrogen reduction treatment was carried out at 450 °C, 30 min and 10 °C min^{-1} using hydrogen gas with $H_2:Ar = 3:1$ (Total 240 SCCM) before the activity test.

2.2 Characterisation

The crystal structures of the two CeO_2 supports were characterised using powder X-ray diffraction (XRD; Smart Lab III; Rigaku Corp.). Measurements were performed using Cu-$K\alpha$ radiation at 40 mA and 40 kV. The diffraction peaks in the range $2\theta = 25–65°$ of the sample were measured at a scanning speed of 0.3° min^{-1}. A monochromator was used for the measurements. The average particle size and dispersion of the supported Ru were calculated using CO pulse measurements (BELCAT-II; Microtrac-Bel Corp.). After 50 mg of sample was placed in the sample tube, the reduction was performed under the following conditions: $H_2:Ar = 3:1$ (total 50 mL min^{-1}), 473 or 873 K, and 2 h. The samples were purged with He. The temperature was then lowered to 323 K with He purging (total 50 mL min^{-1}), maintained for 30 min, and stabilised before measurement. The electronic state of Ce on the 3wt%Ru/CeO_2-p, and -s, surface and number of surface hydroxyl groups were analysed using X-ray photoelectron spectroscopy (PHI VersaProbe 4; ULVAC-PHI Co.). Charge correction was performed based on Ce 3d at 882.3 eV.[31] Before the measurement, a 1 h reduction treatment was conducted in the pre-treatment chamber of the instrument under a flow of $N_2:H_2 = 1:3$ (total 100 mL min^{-1}). The samples were transported from the pre-treatment chamber to the measurement chamber without exposure to air. The spectra were measured at ambient temperature and processed to obtain the background spectra using the Proctor–Sherwood–Shirley method.[32,33] The surface hydroxyl content was calculated using eqn (1).[15]

$$\text{OH ratio} = \frac{(\text{area of OH} + \text{C}-\text{O} + \text{O}-\text{C}=\text{O in O 1s spectra}) - \text{RSF}_{\text{O 1s}}/\text{RSF}_{\text{C 1s}}(\text{area of C}-\text{O} + \text{O}-\text{C}=\text{O in C 1s spectra})}{(\text{area of O}_{\text{lat}}\text{ in O 1s spectra})} \quad (1)$$

For evaluating surface proton migration ability, the surface ion conductivity was measured using electrochemical impedance spectroscopy (EIS) with a two-electrode, four-wire setup connected *via* a ZG4 interface to an Alpha-A high-performance frequency analyser (Novocontrol Technologies). Probostat™ (NORECs AS, Norway) sample holder was used for this purpose. All measurements were performed at a flow rate of 40 mL min^{-1}, amplitude of 0.1 V and frequency range of 10 MHz–10 mHz. Before measurements, N_2 flowed at 773 K as a pre-treatment to remove the surface-adsorbed species. Pre-treatment was performed until the electrical conductivity attained a steady state. Hydrogen pre-treatment was also performed at 873 K for 12 h at an $H_2:N_2 = 3:1$ (total 100 mL min^{-1}). Subsequently, the conductivity was measured at the same gas composition as that in the pre-treatment after a temperature drop to 473 K. The EIS spectra in an H_2 atmosphere were measured after the impedance value at a frequency of 1 Hz attained a steady state at the measurement temperature. The discs used for EIS measurements were made of 1.00 g CeO_2-p, or -s powder and pressed at 90 kN for 30 min. Following

pressing, the discs were pre-sintered at 1173 K and 5 K min^{-1} for 3 h under an air atmosphere. Subsequently, Pt paste was applied to both sides of the pellets and sintered at 1173 K and 5 K min^{-1} for 1 h under an air atmosphere. The relative density of the discs obtained was approximately 60% in both cases. These heat treatments for making EIS samples had little effect on their structures of CeO_2.

2.3 Theoretical calculations

All *ab initio* calculations were performed using the Vienna *Ab initio* Simulation Package (VASP) 6.4.2. The exchange-correlation function was described using the Generalised Gradient Approximation revision Perdew–Burke–Ernzerhof. The electronic states were represented using the projector augmented wave method, and a plane wave basis with a cut-off energy of 400 eV was used for the wave function. The Coulomb interaction of the localised electrons was expressed in Ce 4f with a U parameter of 5 eV. The van der Waals dispersion forces were described using the DFT-D3 of Grimme *et al.*[34–38]

All bulk and surface models were structurally optimised under the following conditions: electron occupation was represented using the first-order Methfessel–Paxton method for the Ru bulk and Gaussian method with sigma set to 0.05 for the other models. The k-points were set in reciprocal lattice space, centred at the Γ point every 0.04 $Å^{-1}$ for the Ru bulk, $5 \times 5 \times 5$ for the CeO_2 bulk and $3 \times 3 \times 1$ for all surface models. SCF calculations were performed until the energy difference between successive iterations was $<10^{-8}$ eV, and structure optimisation was performed until the energy difference between two consecutive structures was $<10^{-5}$ eV.[35–38]

For the model construction, first, bulk models of Ru (16 atoms) and CeO_2 (12 atoms) were structurally optimised to obtain the lattice constants under these calculation conditions. The structure-optimised CeO_2 structure was used to construct a four-layer surface model comprising 192 atoms of CeO_2 (111), (110) and (100), introducing a 15 Å vacuum layer in the z-direction. The bottom two layers were fixed and structurally optimised. Cluster(s) of one, four and ten Ru atom(s) were placed on the resulting surface model and fixed to the same atoms for structural optimisation. However, only one Ru atom was considered for CeO_2 (110).

All energies were obtained by applying tetrahedral electron occupation with Blöchl's correction to the structure-optimised model for the same k-points as in the structure-optimised SCF calculations, which were performed until the energy difference between successive iterations was $<10^{-6}$ eV.

The surface (E_{surf}) and cluster binding (E_{bind}) energies were calculated as follows:

$$E_{surf} = \frac{1}{A}\left(E_{CeO_2(hkl)} - \frac{192}{12}E_{CeO_2\ bulk}\right) \quad (2)$$

$$E_{bind} = E_{Ru_X/CeO_2(hkl)} - E_{Ru_X} - E_{CeO_2(hkl)} \quad (3)$$

where A is the surface index of the $CeO_2(hkl)$ surface, $E_{CeO_2(hkl)}$ is the energy of the $CeO_2(hkl)$ surface model, $E_{CeO_2 bulk}$ is the energy of the CeO_2 bulk model, $E_{Ru_X/CeO_2(hkl)}$ is the energy of the $CeO_2(hkl)$ model carrying the Ru_X atom cluster and E_{Ru_X} is the energy of the Ru_X atoms, calculated using the following equation:

$$E_{Ru_X} = \frac{X}{16}E_{Ru\ bulk} \quad (4)$$

Here, $E_{Ru\ bulk}$ is the energy of the Ru bulk model and E_{Ru_X} is larger than the cluster binding energy because it does not include the surface energy of the Ru cluster itself. Therefore, the positive and negative values of E_{bind} did not correspond to the spontaneity of the cluster.

2.4 Activity tests

The activity tests were performed using an atmospheric-pressure fixed-bed flow reactor. A quartz tube (inner diameter: 6 mmϕ, outer diameter: 8 mmϕ) was used for the reaction tube, and a SUS304 rod (diameter: 2 mmϕ) was used for the electrode. The 100 mg catalyst of 3wt%Ru/CeO_2-s and 3wt%Ru/CeO_2-p was charged in the reactor, and the top and bottom electrodes were inserted to contact the catalyst bed. Moreover, an electric field was applied by passing a DC of 6.0 mA through the catalyst bed with a DC power supply unit. The temperature of the catalyst bed was measured using a thermocouple inserted into the reaction tube, contacting the bottom of the catalyst bed. The response voltage was measured using a digital phosphor oscilloscope (TDS 2001C, Tektronix Inc.). The activity test was conducted under atmospheric pressure, $N_2 : H_2 = 1 : 3$ (total 240 mL min^{-1}), thermal catalytic activities were evaluated at 673 K and catalytic activities in the EF were evaluated at 373–473 K. Reduction treatments were performed before each activity test at 723 K for 2 h under the same atmosphere as the activity tests. The ammonia produced was trapped in distilled water, and its concentration was measured using an ion chromatograph (IC-2001; Tosoh Co., Inc.).

3 Results & discussion

3.1 Differences between CeO_2-p and CeO_2-s crystal structures

First, the structures of CeO_2-p and CeO_2-s were evaluated by various methods. Fig. 1(a) shows that the Ce (111) and (200) planes were observed in both samples. Comparing the proportions of these planes between the samples, more Ce (200) planes were exposed on the CeO_2-p surface (17.2%) than on the CeO_2-s surface. The XRD diffraction spectra were then analysed to confirm each sample's crystallinity and crystal assembly (Fig. 1(b) and Table S1†). No significant peak shifts were observed between the two samples, confirming the absence of crystal stretching caused by the differences in crystallinity. In contrast, focusing on the FWHM, CeO_2-p exhibited a higher crystallinity and larger primary crystallite size than CeO_2-s. Brunauer–Emmett–Teller surface area measurements demonstrated that CeO_2-s had a smaller specific surface area than CeO_2-p (Table S2).† Furthermore, the electron diffraction images confirmed that the crystals of CeO_2-p were oriented in a specific direction (Fig. 1(c) and (d)). These results suggest that while CeO_2-s

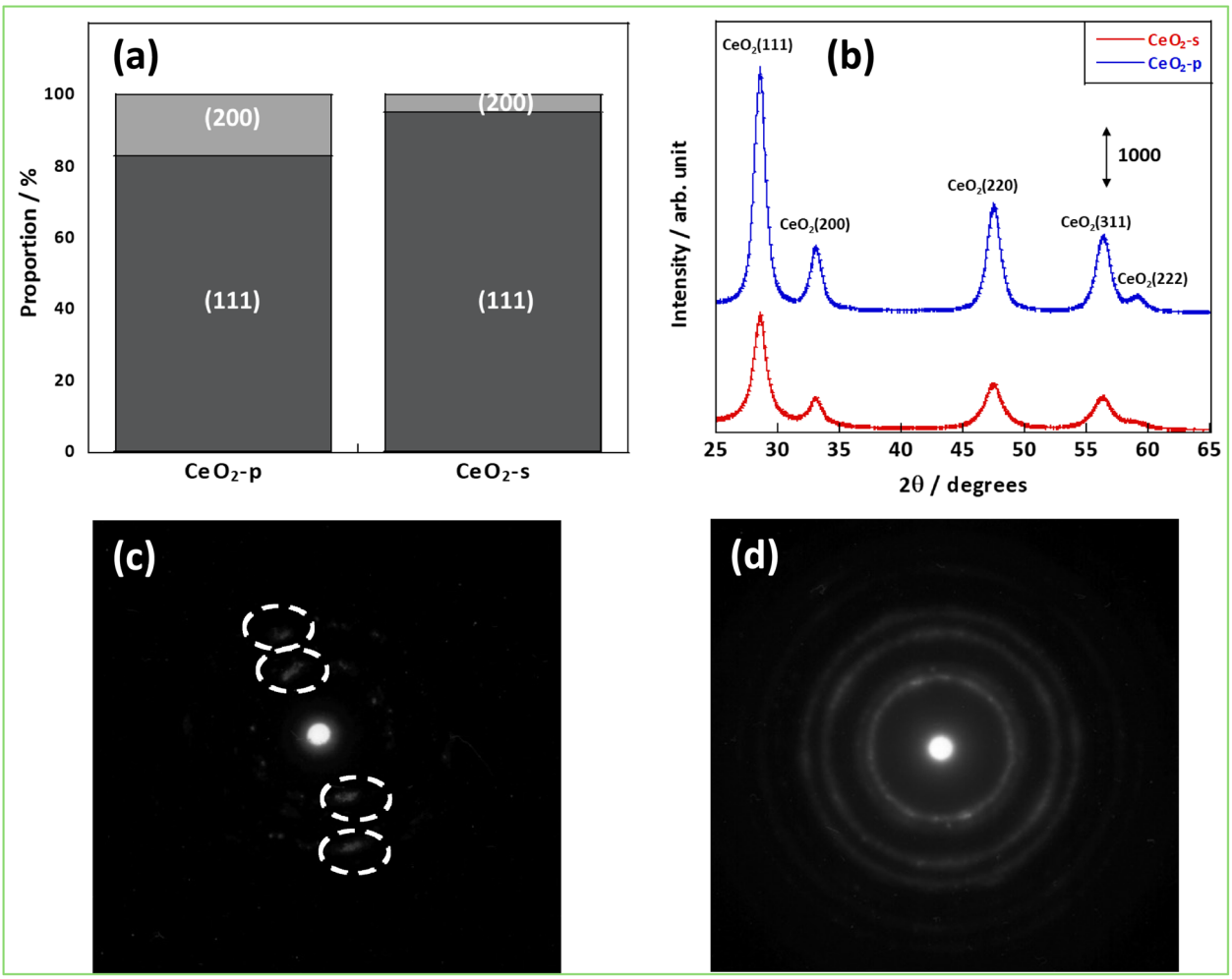

Fig. 1 Structural analysis results; (a) percentage of surfaces exposed, (b) XRD results, (c) electron diffraction image of CeO_2-p, (d) electron diffraction image of CeO_2-s.

comprised smaller primary crystallites than CeO_2-p, its smaller surface area was due to strong secondary crystallisation.

3.2 Evaluation of surface proton conductivity

As mentioned in the introduction, hydrogen spillover is thought to be driven by the forced transfer of electrons due to the application of the DC application in the NH_3 synthesis reaction with an EF, and the amount and conductivity of protons and electrons are significant. Therefore, these parameters were compared for CeO_2-p and CeO_2-s. First, to evaluate the number of conduction electrons and H^+ carriers on the CeO_2-p and CeO_2-s surfaces, the XPS spectra of Ce 3d and O 1s were measured following treatment in an NH_3 synthetic atmosphere. Moreover, the influence of the degree of crystalline aggregation of the support on the electronic state of CeO_2 and the number of surface hydroxyl groups in the reaction atmosphere was investigated. Fig. 2 shows the Ce 3d spectra of each catalyst after the 473 K reduction treatment. The Ce 3d peak shift did not accompany the charge change, and the Ce^{3+} ratio on the surface remained unchanged, regardless of the degree of crystal assembly (Tables S3 and 4†). The ratio of Ce^{3+} after the reaction with the EF was also measured, but no change in the electronic state of Ce was observed between the different catalysts (Fig. S3, Tables S5 and 6†). Hydrogen spillover on CeO_2 is known to conduct electrons owing to the Ce^{4+} and Ce^{3+} redox reactions.[39] Therefore, the proportion of Ce^{3+} corresponded to the carrier concentration of electron conduction at the surface, and this carrier concentration was equal for CeO_2-p and CeO_2-s. The O 1s spectra showed that the number of surface hydroxyl groups on the two catalysts was similar, so the amount of H^+ carriers (*i.e.* OH groups) did not change with crystallinity (Fig. 3). Therefore, the electrons and protons, which are the species that couple and conduct in the spillover, were aligned in CeO_2-p and CeO_2-s.

The conductivity of carriers, such as electrons and protons, in the presence of an EF within an NH_3 synthetic atmosphere (473 K, H_2/N_2 = 3/1, total 40 mL min^{-1}) was then investigated using EIS measurements. Generally, hydrogen diffusivity in CeO_2 is low, and CeO_2 requires considerably high temperatures (>1050 K) to exhibit bulk carrier conduction.[40,41] Because the measurement temperature was 473 K, the bulk conduction of hydrogen did not occur, and the carriers were conducted on the surface and grain boundaries *via* a hopping mechanism.

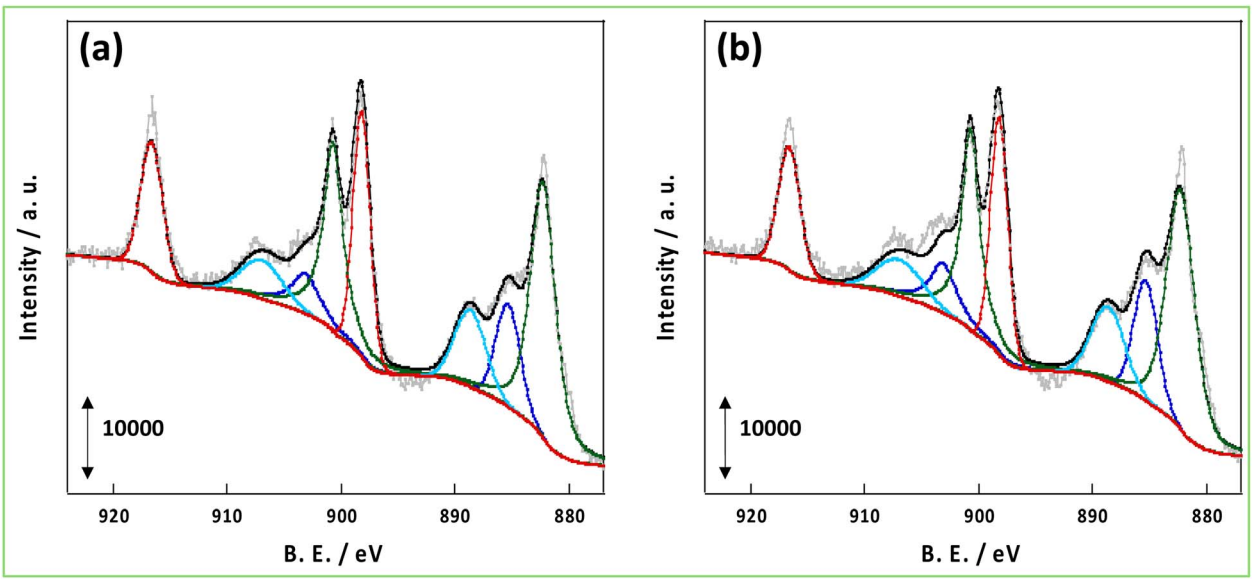

Fig. 2 XPS spectra of Ce 3d after pre-treatment at 473 K; (a) 3wt%Ru/CeO_2-p, (b) 3wt%Ru/CeO_2-s.

Because the diameter of the circle in the Nyquist plot of the EIS measurement corresponds to the resistivity component, the ionic conductivity of CeO_2-p was relatively high at 473 K and under a hydrogen atmosphere (Fig. 4). The resistivity of the grain boundary was higher than that of the bulk material. The inhibition of conduction was more pronounced at low temperatures, as observed in the present study. Space charge layers at the grain boundaries increase the grain boundary resistivity and inhibit ion transport.[42,43] The stability of excess charge localisation on the CeO_2 surface depended on the face index of the exposed surface.[44] Therefore, the more uniform the exposed surfaces and surface orientation of CeO_2, the higher the probability of contact between identical surfaces at the grain boundaries. This suppresses the formation of space charge layers and reduces grain boundary resistance. Therefore, CeO_2-p exhibited a relatively higher conductivity than CeO_2-s because of the alignment of the exposed surfaces and orientations. Thus, the conductivity can be improved by controlling the crystallinity even using the same pure material.

3.3 Effect of support structures on CeO_2–Ru interaction

The catalyst support binds the impregnated metal as a heterogeneous catalyst, thereby inhibiting the aggregation of active metals during the reaction is crucial for keeping higher dispersion of supported metal. To evaluate the influence of the

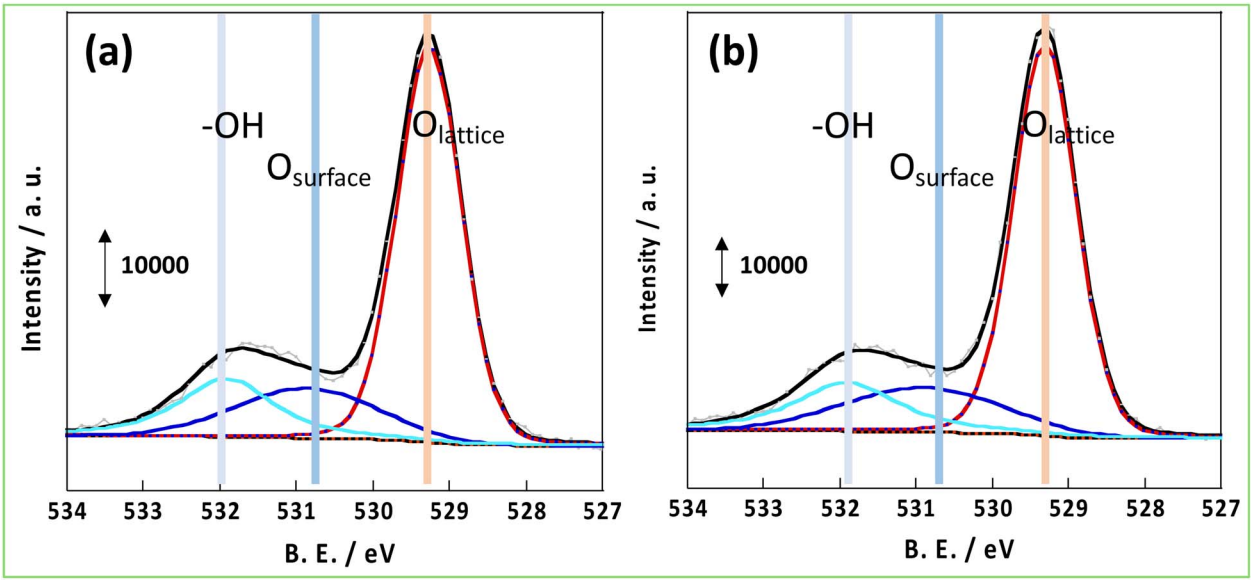

Fig. 3 XPS spectrum of O 1s after pre-treatment at 473 K; (a) 3wt%Ru/CeO_2-p, (b) 3wt%Ru/CeO_2-s.

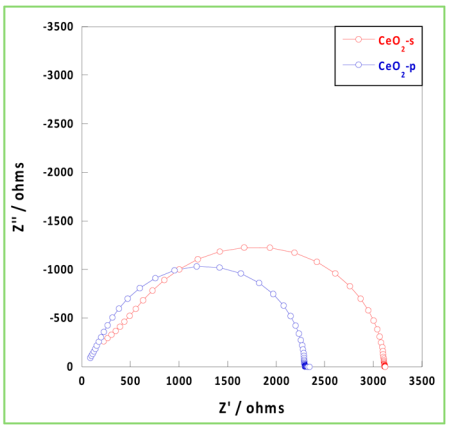

Fig. 4 Nyquist plot at 473 K under NH_3 synthetic atmosphere.

crystallinity of each support on the support–metal interaction, CO pulse measurements were performed, and the dispersion and average particle size of Ru were observed. Table 1 shows that the Ru particle size in CeO_2-s increased nearly five-fold when the pretreatment temperature was increased from 473 to 873 K, whereas in CeO_2-p, the increase was approximately two. This indicates that the binding strength of the Ru particles differed between CeO_2-s and CeO_2-p. The energy of a solid surface is strongly related to particle binding. Therefore, the surface energies and binding energies of the Ru clusters were calculated from first principles for the (111) and (100) surfaces, which were observed in the previous section, and for the (110) surface, which is known as a metastable surface. The results show that the surface energies were of the same order as those previously reported: (111) < (110) < (100). Furthermore, the binding energies of the clusters of one Ru atom on these surfaces were in the order (100) < (111) < (110). Thus, the (100) surface was more Ru-bound than the (111) surface, and CeO_2-s was less likely to aggregate Ru particles than CeO_2-p because of the higher proportion of (100) surfaces. Furthermore, the (110) surface energy, which was lower than that of the (111) surface, exhibited weaker binding than the (111) surface, indicating that CeO_2-s with a (100) surface, instead of a (110) surface, was important for suppressing aggregation. The binding energies were also determined for Ru 4- and 10-atom clusters to investigate the tendency of multiple Ru and O atoms on the surface to bind. The results showed that the trend towards the stronger binding of Ru clusters on the (100) surface than on the (111) surface was maintained, even when the number of binding sites increased (Table 2).

Table 1 Ru particle size of each catalyst

Sample	Pretreatment temperature/K	Metal dispersion/%	Ru particle size/nm
3wt%Ru/CeO_2-s	473	52.9	2.54
	873	11.4	11.8
3wt%Ru/CeO_2-p	473	88.1	1.52
	873	43.9	3.05

Table 2 Binding energies of Ru atoms and clusters on CeO_2 surfaces

Miller index	Surface energies/eV $Å^{-2}$	$E_{bindRu1}$/eV	$E_{bindRu4}$/eV	$E_{bindRu10}$/eV
(111)	0.12	1.69	9.15	19.6
(110)	0.18	2.01	—	—
(100)	0.25	0.8	5.01	16.4

3.4 Impact of support effects on NH_3 synthesis with an EF

Based on the characterisation and theoretical calculations described above, improved ionic conductivity and strong CeO_2–Ru interactions were achieved by controlling the crystalline assembly of the supports. The catalytic performances of these supports were evaluated by performing NH_3 synthesis using an DC-EF. Fig. 5 shows the NH_3 synthesis activity in the temperature-change tests in an electric field. Based on these results, NH_3 synthesis activity with an EF was enhanced when CeO_2-p was used as the catalyst support. The turnover frequency normalised to the metal perimeter (TOF-p), which indicates the catalytic performance at the active sites situated at the metal–support interface, was calculated (eqn (5)). CeO_2-p was superior to CeO_2-s in NH_3 synthesis with an EF because of its high ionic conductivity, even when the effect of Ru was excluded (Table 3).

$$\text{TOF-p}\ [s^{-1}] = \frac{\text{number of moles of converted } N_2}{\text{number of metal atoms at perimeter}} \quad (5)$$

The NH_3 reaction with an EF proceeded *via* a mechanism different from that of the conventional thermal reaction, and the reaction proceeded in parallel with the thermal reaction when an EF was applied. Therefore, to visualise the effect of an EF, we considered both the EF and thermal reactions. Arrhenius plots were made based on the catalytic performances obtained from the catalytic reactions in an electric field and thermal

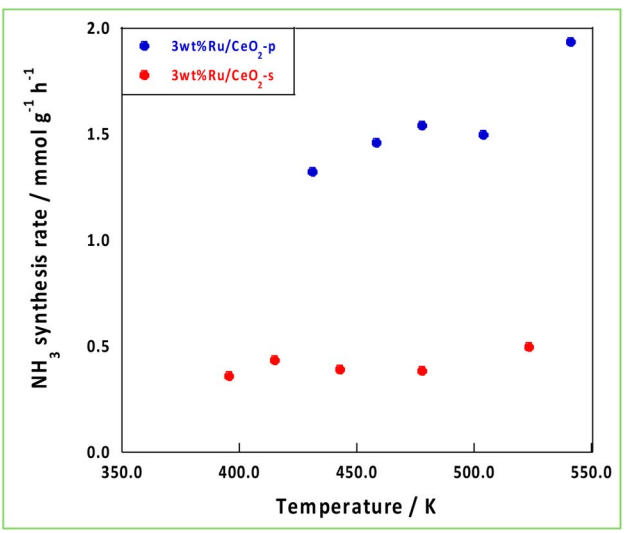

Fig. 5 Temperature variation test in the EF.

Table 3 Comparison of NH_3 synthesis activity in the EF and TOF-p

Sample	Temperature/K	Response voltage/kV	NH_3 synthesis rate/mmol g^{-1} h^{-1}	NH_3 synthesis rate/mmol g^{-1} h^{-1} W^{-1}	TOF-p/s^{-1}
3wt%Ru/CeO_2-s	470	0.168	0.390	0.387	0.00832
3wt%Ru/CeO_2-p	478	0.389	1.54	0.660	0.0118

reactions in the temperature range where the thermal reaction was not dominant. Subsequently, the activation energies were compared. Fig. 6 shows the Arrhenius plots generated by the temperature change during the tests. These results demonstrate that the apparent activation energies of the two catalyses were comparable when the effect of the EF was eliminated. However, in the presence of an EF, the Arrhenius plots revealed that CeO_2-p proceeded with a lower apparent activation energy than did CeO_2-s in the specified temperature range (Fig. 7). This result clearly indicates that the ionic conductivity obtained by

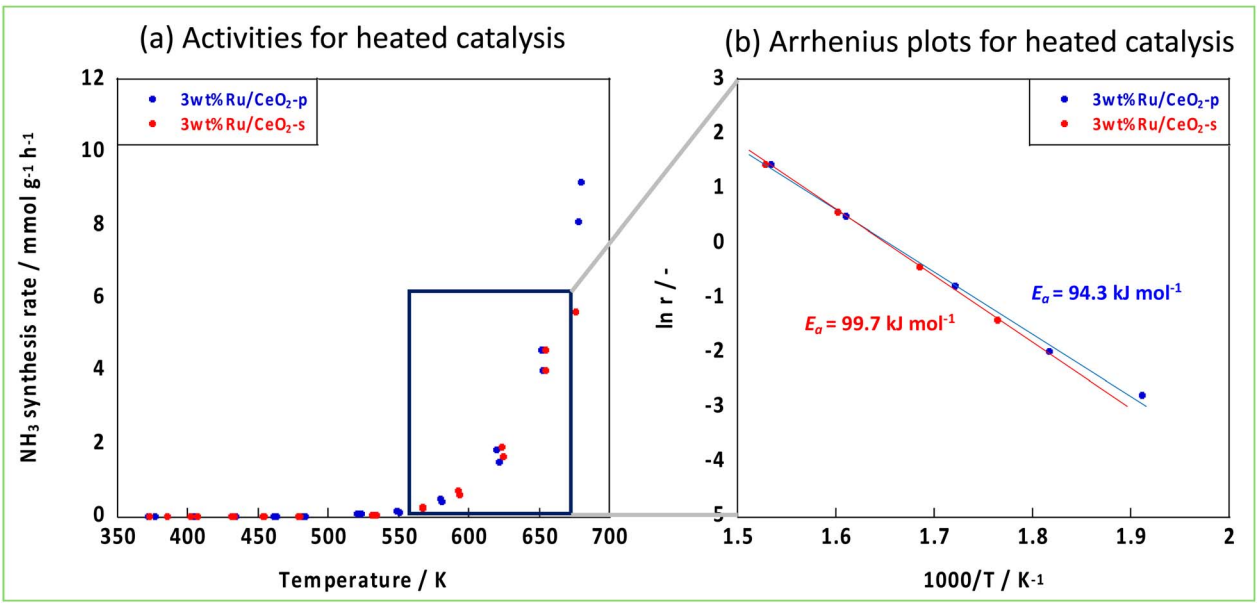

Fig. 6 Activities of two Ru-catalysts supported on different CeO_2 supports, (a) activities for heated catalysis, (b) Arrhenius plots.

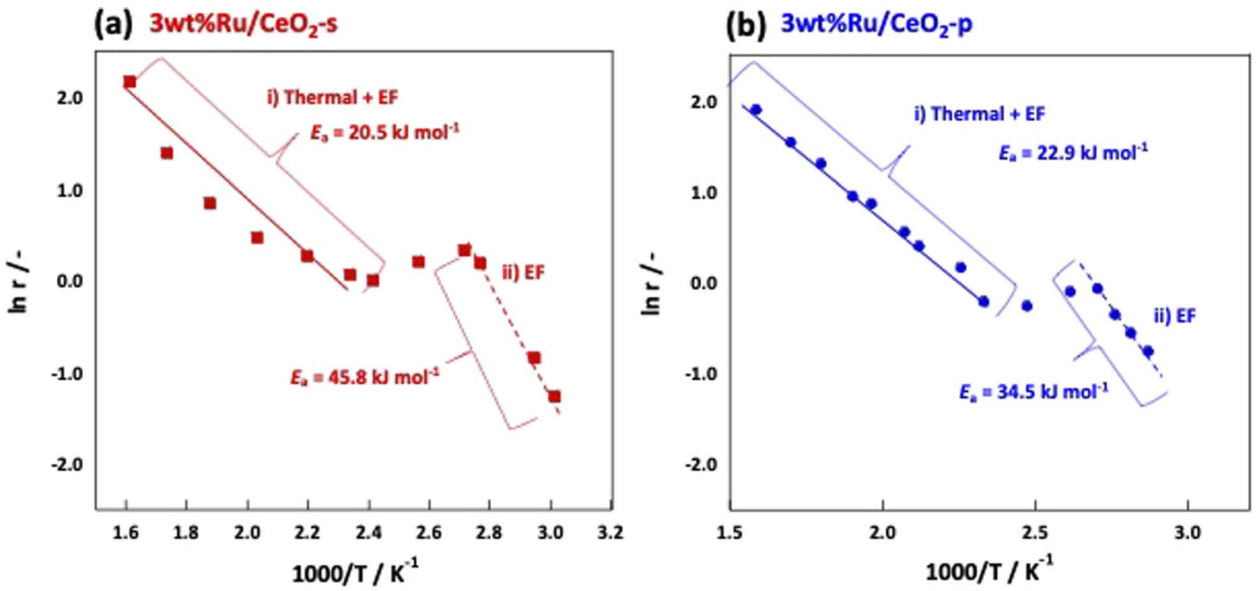

Fig. 7 Arrhenius plots when an electric field is applied to (a) 3wt%Ru/CeO_2-s, (b) 3wt%Ru/CeO_2-p.

controlling the crystal assembly lowered the activation barrier for NH_3 synthesis with the EF. Fig. 7 also suggests that the temperature range at which switching from the EF reaction to the thermal reaction is similar for the two catalyses, and the surface hydroxyl groups are uniform during the reaction. As observed in the activity and Arrhenius plots, controlling the crystal assembly improved the surface ionic conductivity and enhanced the formation of N_2H intermediates, thus increasing the activity per active site of the reaction and lowering the apparent activation energy.

4 Conclusion

Herein, the influences of the degree of crystal aggregation of CeO_2 on the support properties and NH_3 synthesis activity of an EF were investigated. CeO_2-p had a high crystal orientation, and numerous CeO_2 (100) planes were exposed. CeO_2-p had a high ion conductivity, and it may be attributed to the reduced grain boundary resistance owing to the highly crystalline orientation. This result indicates that the trade-off between ion-conducting carrier quantity and mobility in surface proton conduction under an EF, which can be regarded as current-induced hydrogen spillover, can be promoted by controlling the crystal assembly. Furthermore, Ru aggregation was controlled by suppressing the secondary crystallisation of CeO_2. This phenomenon is attributed to the strong binding of Ru to the CeO_2 (100) surface, which was exposed in large numbers to the CeO_2 crystalline surface. The high proton conductivity and strong Ru–CeO_2 interactions obtained by suppressing crystal aggregation resulted in an increase in the activity of NH_3 synthesis in an EF at low temperatures.

Conflicts of interest

There are no conflicts to declare.

Acknowledgements

All the catalysts used in this study were prepared and supplied by Mitsui Mining and Smelting Co., Ltd. Electron diffraction observations were conducted using equipment (JEM-2100F: Material Characterization Central Laboratory in Waseda University) shared with the MEXT Project for Promoting Public Utilization of Advanced Research Infrastructure (Program for supporting the construction of core facilities) under grant numbers JPMXS0440500022 and JPMXS0440500023. This study was partly conducted using a supercomputer system at the Information Initiative Centre, Hokkaido University, Sapporo, Japan.

References

1 M. Yue, H. Lambert, E. Pahon, R. Roche, S. Jemei and D. Hissel, *Renewable Sustainable Energy Rev.*, 2021, **146**, 111180.
2 R. H. Lin, Y. Y. Zhao and B. D. Wu, *Int. J. Hydrogen Energy*, 2020, **45**, 20164–20175.
3 Y. Sekine and T. Higo, *Top. Catal.*, 2021, **64**, 470–480.
4 Y. Kobayashi, Y. Tang, T. Kageyama, H. Yamashita, N. Masuda, S. Hosokawa and H. Kageyama, *J. Am. Chem. Soc.*, 2017, **139**, 18240–18246.
5 R. Manabe, H. Nakatsubo, A. Gondo, K. Murakami, S. Ogo, H. Tsuneki, M. Ikeda, A. Ishikawa, H. Nakai and Y. Sekine, *Chem. Sci.*, 2017, **8**, 5434–5439.
6 K. Murakami, R. Manabe, H. Nakatsubo, T. Yabe, S. Ogo and Y. Sekine, *Catal. Today*, 2018, **303**, 271–275.
7 K. Murakami, Y. Tanaka, S. Hayashi, R. Sakai, Y. Hisai, Y. Mizutani, A. Ishikawa, T. Higo, S. Ogo, J. G. Seo, H. Tsuneki, H. Nakai and Y. Sekine, *J. Chem. Phys.*, 2019, **151**, 064708.
8 K. Murakami, Y. Tanaka, R. Sakai, Y. Hisai, S. Hayashi, Y. Mizutani, T. Higo, S. Ogo, J. G. Seo, H. Tsuneki and Y. Sekine, *Chem. Commun.*, 2020, **56**, 3365–3368.
9 K. Murakami and Y. Sekine, *Phys. Chem. Chem. Phys.*, 2020, **22**, 22852.
10 K. Shun, K. Mori, S. Masuda, N. Hashimoto, Y. Hinuma, H. Kobayashi and H. Yamashita, *Chem. Sci.*, 2022, **13**, 8137–8147.
11 W. Karim, A. Kleibert, U. Hartfelder, A. Balan, J. Gobrecht, J. A. van Bokhoven and Y. Ekinci, *Sci. Rep.*, 2016, **6**, 18818.
12 R. Sakai, K. Murakami, Y. Mizutani, Y. Tanaka, S. Hayashi, A. Ishikawa, T. Higo, S. Ogo, H. Tsuneki, H. Nakai and Y. Sekine, *ACS Omega*, 2020, **5**(12), 6846–6851.
13 Y. Tanaka, K. Murakami, S. Doi, K. Ito, K. Saegusa, Y. Mizutani, S. Hayashi, T. Higo, H. Tsuneki, H. Nakai and Y. Sekine, *RSC Adv.*, 2021, **11**, 7621–7626.
14 K. Murakami, Y. Mizutani, H. Sampei, A. Ishikawa and Y. Sekine, *J. Chem. Phys.*, 2021, **154**, 164705.
15 K. Murakami, Y. Mizutani, H. Sampei, A. Ishikawa, Y. Tanaka, S. Hayashi, S. Doi, T. Higo, H. Tsuneki, H. Nakai and Y. Sekine, *Phys. Chem. Chem. Phys.*, 2021, **23**, 4509–4516.
16 M. Kitano, Y. Inoue, Y. Yamazaki, F. Hayashi, S. Kanbara, S. Matsuishi, T. Yokoyama, S. W. Kim, M. Hara and H. Hosono, *Nat. Chem.*, 2012, **4**, 934–940.
17 M. Kitano, S. Kanbara, Y. Inoue, N. Kuganathan, P. V. Sushko, T. Yokoyama, M. Hara and H. Hosono, *Nat. Commun.*, 2015, **6**, 6731.
18 T. Montini, M. Melchionna, M. Monai and P. Fornasiero, *Chem. Rev.*, 2016, **116**, 5987–6041.
19 J. G. Nunan, H. J. Robota, M. J. Cohn and S. A. Bradley, *J. Catal.*, 1992, **133**, 309–324.
20 D. Andreeva, V. Idakiev, T. Tabakova, L. Ilieva, P. Falaras, A. Bourlinos and A. Travlos, *Catal. Today*, 2002, **72**, 51–57.
21 A. Goguet, F. C. Meunier, D. Tibiletti, J. P. Breen and R. Burch, *J. Phys. Chem. B*, 2004, **108**, 20240–20246.
22 I. I. Soykal, H. Sohn and U. S. Ozkan, *ACS Catal.*, 2012, **2**, 2335–2348.
23 I. I. Soykal, B. Bayrama, H. Sohna, P. Gawadea, J. T. Miller and U. S. Ozkan, *Appl. Catal., A*, 2012, **449**, 47–58.
24 S. Carrettin, P. Concepcion, A. Corma, J. M. L. Nieto and V. F. Puntes, *Angew. Chem., Int. Ed.*, 2004, **43**, 2538–2540.
25 Q. Li, Y. Zhang, G. Chen, J. Fan, H. Lan and Y. Yang, *J. Catal.*, 2010, **273**, 167–176.

26 C. Li, Y. Shi, Z. Zhang, J. Ni, X. Wang, J. Lin, B. Lin and L. Jiang, *J. Energy Chem.*, 2021, **60**, 403–409.
27 F. Wang, C. Li, X. Zhang, M. Wei, D. G. Evans and X. Duan, *J. Catal.*, 2015, **329**, 177–186.
28 M. Nolan and G. W. Watson, *J. Phys. Chem. B*, 2006, **110**, 16600–16606.
29 B. Lin, Y. Liu, L. Heng, X. Wang, J. Ni, J. Lin and L. Jiang, *Ind. Eng. Chem. Res.*, 2018, **57**, 9127–9135.
30 Z. Ma, S. Zhao, X. Pei, X. Xionga and B. Hu, *Catal. Sci. Technol.*, 2017, **7**, 191.
31 N. Nakano, M. Torimoto, H. Sampei, R. Yamashita, R. Yamano, K. Saegusa, A. Motomura, K. Nagakawa, H. Tsuneki, S. Ogo and Y. Sekine, *RSC Adv.*, 2022, **12**, 9036–9043.
32 A. Proctor and P. M. A. Sherwood, *Anal. Chem.*, 1982, **54**(1), 13–19.
33 D. A. Shirley, *Phys. Rev. B*, 1972, **5**(12), 4709.
34 S. Grimme, J. Antony, S. Ehrlich and S. Krieg, *J. Chem. Phys.*, 2010, **132**, 154104.
35 M. D. Krcha, A. D. Mayernick and M. J. Janik, *J. Catal.*, 2012, **293**, 103–115.
36 H. T. Chen and J. G. Chang, *J. Chem. Phys.*, 2010, **132**, 214702.
37 A. D. Mayernick and M. J. Janik, *J. Phys. Chem. C*, 2008, **112**(38), 14955–14964.
38 M. B. Watkins, A. S. Foster and A. L. Shluger, *J. Phys. Chem. C*, 2007, **111**(42), 15337–15341.
39 A. Beck, D. Kazazis, Y. Ekinci, X. Li, E. A. M. Gubler, A. Kleibert, M. G. Willinger, L. Artiglia and J. A. van Bokhoven, *ACS Nano*, 2023, **17**, 1091–1099.
40 Y. Nigari, K. Kawamura, T. Kawada, J. Mizusaki and M. Ishigame, *J. Electrochem. Soc.*, 1999, **146**, 2948–2953.
41 T. Matsuda, R. Ishibashi, Y. Koshizuka, H. Tsuneki and Y. Sekine, *Chem. Commun.*, 2022, **58**, 10789–10792.
42 X. Guo and J. Maier, *J. Electrochem. Soc.*, 2001, **148**, E121.
43 X. Guo, W. Sigle and J. Maier, *J. Am. Ceram. Soc.*, 2003, **86**, 77–87.
44 P. P. Bailac, P. G Lustemberg and M. V. G. Pirovano, *J. Phys.: Condens. Matter*, 2021, **33**, 504003.